AGU PUBLICATIONS

JGR

Journal of Geophysical Research: Oceans

RESEARCH ARTICLE

10.1002/2016JC012225

Key Points:
- Argo data and altimetry reveal systematic eddy perturbations to mixed-layer depth (MLD) across the Southern Ocean
- Eddy MLD signals, shallow in cyclones, deep in anticyclones, increase with seasonal background MLD and with eddy amplitude
- Asymmetry in eddy-induced MLD signals yields a small but detectable net MLD deepening

Supporting Information:
- Supporting Information S1

Correspondence to:
U. Hausmann,
uhausc@gmail.com

Citation:
Hausmann, U., D. J. McGillicuddy, and J. Marshall (2017), Observed mesoscale eddy signatures in Southern Ocean surface mixed-layer depth, *J. Geophys. Res. Oceans*, *122*, 617–635, doi:10.1002/2016JC012225.

Received 8 AUG 2016
Accepted 14 DEC 2016
Accepted article online 26 DEC 2016
Published online 27 JAN 2017

Observed mesoscale eddy signatures in Southern Ocean surface mixed-layer depth

U. Hausmann[1,2], Dennis J. McGillicuddy Jr.[1], and John Marshall[2]

[1]Department of Applied Ocean Physics and Engineering, Woods Hole Oceanographic Institution, Woods Hole, Massachusetts, USA, [2]Department of Earth Atmospheric and Planetary Sciences, Massachusetts Institute of Technology, Cambridge, Massachusetts, USA

Abstract Combining satellite altimetry with Argo profile data a systematic observational estimate of mesoscale eddy signatures in surface mixed-layer depth (MLD) is provided across the Southern Ocean (SO). Eddy composite MLD anomalies are shallow in cyclones, deep in anticyclones, and increase in magnitude with eddy amplitude. Their magnitudes show a pronounced seasonal modulation roughly following the depth of the climatological mixed layer. Weak eddies of the relatively quiescent SO subtropics feature peak late-winter perturbations of $\pm$10 m. Much larger MLD perturbations occur over the vigorous eddies originating along the Antarctic Circumpolar Current (ACC) and SO western boundary current systems, with late-winter peaks of $-$30 m and $+$60 m in the average over cyclonic and anticyclonic eddy cores (a difference of $\approx$ 100 m). The asymmetry between modest shallow cyclonic and pronounced deep anticyclonic anomalies is systematic and not accompanied by corresponding asymmetries in eddy amplitude. Nonetheless, the net deepening of the climatological SO mixed layer by this asymmetry in eddy MLD perturbations is estimated to be small (few meters). Eddies are shown to enhance SO MLD variability with peaks in late winter and eddy-intense regions. Anomalously deep late-winter mixed layers occur disproportionately within the cores of anticyclonic eddies, suggesting the mesoscale heightens the frequency of deep winter surface-mixing events along the eddy-intense regions of the SO. The eddy modulation in MLD reported here provides a pathway via which the oceanic mesoscale can impact air-sea fluxes of heat and carbon, the ventilation of water masses, and biological productivity across the SO.

1. Introduction

The ocean's surface mixed layer determines the volume of the global ocean in direct contact with the atmosphere. It mediates all exchange between the atmosphere and the subsurface ocean, and its properties directly condition air-sea fluxes in variables such as heat and carbon. The depth of the mixed layer determines how far surface mixing reaches down entraining properties from below, and thus is one of several key variables setting the properties of the mixed layer. This depth shows large seasonal variations, which give rise to the stratified seasonal thermocline below the shallow summer mixed layer and down to the level of deepest winter mixing, defining the top of the permanent thermocline. The ocean's mixed layer features pronounced geographical variations in depth, reflecting spatial variations in atmospheric wind and buoyancy forcing, but also advection by ocean currents. Deepest mixed-layer depths occur during polar winter convection, and also equatorward of mid-latitude western boundary currents and their separations, as well as equatorward of the Antarctic Circumpolar Current in the Southern Ocean.

Much progress has been made in the observational knowledge of these large-scale climatological variations in mixed-layer depth [e.g., *de Boyer Montégut et al.*, 2004] and the processes responsible for them. The energetic variability in the ocean's circulation also perturbs the surface mixed layer and its depth, in particular at the scale at which its kinetic energy peaks, the oceanic mesoscale at $\approx$ 100 km [*Gill et al.*, 1974; *Scott and Wang*, 2005; *Ferrari and Wunsch*, 2009]. This has long been known, as informed by theory and process modeling studies [e.g., *Klein and Hua*, 1988], as well as occasional in situ field campaigns. These include in particular investigations of Gulf Stream rings and mesoscale features across the North Atlantic and their impacts on air-sea interactions [e.g., *Vastano et al.*, 1980; *Ring Group*, 1981; *Schmitt and Olson*, 1985; *Joyce and Stalcup*, 1985; *Dewar*, 1986; *Williams*, 1988], but also studies in Drake passage [e.g., *Joyce et al.*, 1981]. The oceanic circulations on mesoscales, and also beyond on sub-mesoscales [*Mahadevan*, 2016], induce

mixed-layer depth variations on spatial scales that are smaller than those typical of the buoyancy-flux and wind-forced perturbations resulting from atmospheric synoptic variability ($\approx$ 1000 km). They give rise to mesoscale modulations in surface-layer carbon concentrations, air-sea fluxes, nutrient availability, and oceanic productivity, as examined in a multitude of studies of mesoscale impacts on oceanic biology and biogeochemistry (e.g., reviewed recently by *McGillicuddy* [2016]). The arising mesoscale gradients in mixed-layer depth, in association with mesoscale circulations, furthermore modulate the exchange of properties between the surface layer and the deep ocean [e.g., *Sallée et al*., 2010a].

Observational characterizations of mesoscale signatures in mixed-layer depth have been typically limited to single event field campaigns (see the studies mentioned above). In contrast, satellite observational oceanography has facilitated a range of systematic studies of mesoscale signals in variables measurable from the surface, such as temperature [*Hausmann and Czaja*, 2012], chlorophyll [*Gaube et al*., 2014], ocean-atmosphere coupling and air-sea exchanges [*Chelton et al*., 2004; *O'Neill et al*., 2012; *Frenger et al*., 2013; *Villas Bôas et al*., 2015], and sea surface height, the latter allowing for a dynamical characterization of mesoscale features for the global ocean [e.g., *Chelton et al*., 2011].

Systematic studies of mixed-layer depth are becoming possible with the growing coverage and length of the Argo profile observational archive. Some studies started to make use of this to analyze mesoscale perturbations in surface mixing, locally for the South Indian Ocean [*Gaube et al*., 2013; *Dufois et al*., 2014], and very recently also for the subtropical ocean gyres of the global ocean [*Dufois et al*., 2016]. Here we exploit the Argo archive in combination with satellite altimetry, processed into a global atlas of eddying features and their characteristics [*Chelton et al*., 2011], to provide a systematic characterization of observed mesoscale signatures in mixed-layer depth for the traditionally sparsely observed Southern Ocean.

Argo-profile observations have been crucial in informing our knowledge of the Southern Ocean mixed-layer depth field, which was previously based only on shipboard measurements. In particular, they have allowed for a much higher resolution characterization of the observed climatology of mixed-layer depth [*de Boyer Montégut et al*., 2004; *Dong et al*., 2008; *Schmidtko et al*., 2013], and for investigation into the signatures of interannual variability in mixed-layer depth [*Sallée et al*., 2010b]. So far, a systematic characterization of the signatures of the intense Southern Ocean mesoscale circulations in mixed-layer depth has not been undertaken and is the main goal of the present study. We will establish typical eddy signatures, and provide characterization of their geographical and seasonal variation across the Southern Ocean. We focus in particular on the region of intense eddy variability associated with the Antarctic Circumpolar Current (ACC), in the winter time, when some of the world's deepest mixed layers are formed along this current system and on its equatorward flank. Notably, our analysis is not solely restricted to very energetic nonlinear mesoscale features that can be long-lived, trapping, and transporting their own ecosystems over long distances and times. It also includes the full spectrum of mesoscale circulations, of which short-lived and small-amplitude features constitute the most frequent population [*Chelton et al*., 2011; *Hausmann and Czaja*, 2012; *Frenger et al*., 2015]. Note that Argo float coverage is not typically sufficient to provide a characterization of the evolution of anomalies within individual eddies over their lifetime. Here we thus adopt an approach that characterizes composite eddy snapshots and their associated mixed-layer perturbations, with lifetimes of the latter hypothesized to be similar to those of the associated eddies (weeks to years). We also explore whether the eddy signals average out or whether they give rise to net long-term larger-scale modulations in the depth, variability, and properties of the Southern Ocean surface mixed layer.

The paper is set out as follows. Section 2 introduces the key methods and data sets employed. The available data coverage is assessed, and an overview of mesoscale eddy circulations and the climatological patterns and seasonal evolution of mixed-layer depth across the Southern Ocean (SO) provided. Section 3 presents the key observational results, which characterize the observed variability in mixed-layer depth and eddy signals therein (section 3.1). Section 3.2 addresses the seasonal and geographical variations of the detected mesoscale signatures in SO mixed-layer depths. The implications of these observational results are discussed in section 4, by addressing three key questions: Do eddies have a rectified impact on the mean state of SO mixed-layer depth (section 4.1), on its variability (section 4.2), and do they modulate the frequency of occurrence of deep winter mixed layers (section 4.3)? Conclusions and further discussion are provided in section 5.

2. Southern Ocean Eddy and Mixed-Layer Data sets, Coverage, and Climatologies

Mesoscale eddies are identified as closed contours in spatially high-pass filtered sea surface height (SSH) from Aviso's two-altimeter reference series by an automated algorithm that also tracks eddies from week to week. This results in a global data set of mesoscale eddy tracks (with lifetimes of at least 4 weeks and amplitudes of at least 1 cm) described in detail by *Chelton et al*. [2011, CSS11 hereafter]. Here an updated version of the data set is used as available at http://cioss.coas.oregonstate.edu/eddies/ (third release). The $10\frac{2}{3}$ year timespan from the start of the Argo era in the SO (August 2001) up to the end of the eddy track data set (4 April 2012) is used for the main analyses in this paper. Eddies captured in this data set are seen to be ubiquitous across the entire open SO equatorward of the sea-ice edge and away from continental shelves and plateaus (Figure 1a). They partition into roughly equal numbers of cyclones and anticyclones, characterized respectively by lows and highs in sea level (Table 1). Those eddies with tracked lifetimes longer than 4 months are typically nonlinear (with ratios of eddy rotational to translational speeds greater than unity, see CSS11), and thus able to trap and carry water parcels with them. Note however that identified eddies do not necessarily correspond to closed streamlines in the absolute surface flow. The latter are given by closed contours in full sea level, which is the sum of the high-pass filtered sea level anomalies (whose closed contours are used to identify eddies) plus the filtered anomalies of larger spatial scale (with typically weak associated gradients and flow) and the absolute dynamic topography (to which the altimeter sea level anomalies are referenced). In this context, wave-like features such as transient meanders in absolute dynamic topography can also manifest as closed contours in filtered sea level anomalies. Here all features with closed contours of sea level anomaly are referred to as eddies. Their radii r_e typically lie between 60 and 100 km (not shown). Eddy amplitudes in SSH (mapped in Figure 1b) are seen to vary from less than 5 cm in subtropical basin interiors, steeply increasing to beyond 10 cm approaching western boundary current systems and the ACC jets, and exceeding 30 cm especially along the Agulhas return current (ARC). This spatial pattern in eddy amplitude agrees well with that of the local standard deviation of SSH, which itself primarily reflects the SO eddy kinetic energy distribution. The 10 cm isoline of the SSH standard deviation is indicated by the black contour in Figure 1, based on weekly delayed-time reference series sea level anomalies, as obtained from www.aviso.altimetry.fr, here for the 10 year period 1999–2009.

It is of use to introduce two contrasting oceanic regimes: (i) the regions of intense eddy variability associated with the SO's major current systems, and (ii) the regions of weak eddy variability, such as encountered in the quiescent eastern parts of the subtropical gyres. Here "energetic" regions of the ACC and SO western boundary currents (i) are identified by imposing a lower bound on SSH standard deviation of 10 cm (within the solid contour in Figure 1). An example of the "quiescent" regions (ii) is provided by the South Pacific (SP) east of 150°W, equatorward of 48°S (as outlined by the dashed box in Figure 1). The locations of weekly eddy snapshots whose tracks originate in either of these two regions are color-coded in Figure 1a (see legend). Table 1 provides a census of these eddies; their amplitudes average to 3.5 cm in the quiescent regime, and to 15 cm in the energetic regime (Table 2).

Individual Argo profile surface mixed-layer depths h are estimated based on a density threshold criterion (as in *de Boyer Montégut et al*. [2004]). To assess sensitivity of results to this criterion, mixed layers obtained with the density-based algorithm of *Holte and Talley* [2009] are also examined. These data sets are provided by *Holte et al*. [2010, available online at http://mixedlayer.ucsd.edu]. Here analysis is restricted to profiles to which delayed-time processing has been applied and which are collected prior to the end of the eddy data set. Figure 1c maps resulting profile locations across the SO.

To facilitate the study of mixed-layer depth variability and the eddy signal therein, h of individual profiles is separated into a component reflecting its seasonally-varying climatology and a departure from it, $h=\bar{h}+h'$. For a given profile i, $\bar{h}$ is estimated as the average of h over the $N_c=100$ surrounding profiles j, selected so as to minimize the weight

$$w_{ij}=exp\left\{-\left(\frac{\delta\bar{t}_{ij}^2}{\delta t_c^2}+\frac{\Delta x_{ij}^2}{L_{x_c}^2}+\frac{\Delta y_{ij}^2}{L_{y_c}^2}\right)\right\}. \quad (1)$$

Here $\delta\bar{t}_{ij}$, Δx_{ij}, and Δy_{ij} are the distances between floats in time of year (year day, including all years available), longitude and latitude, and their respective weight in the selection is set via the choice of the time and space scales δt_c, L_{x_c}, and L_{y_c}, set here to 30 days (of the year, i.e., cyclical), 5° longitude and 2° latitude

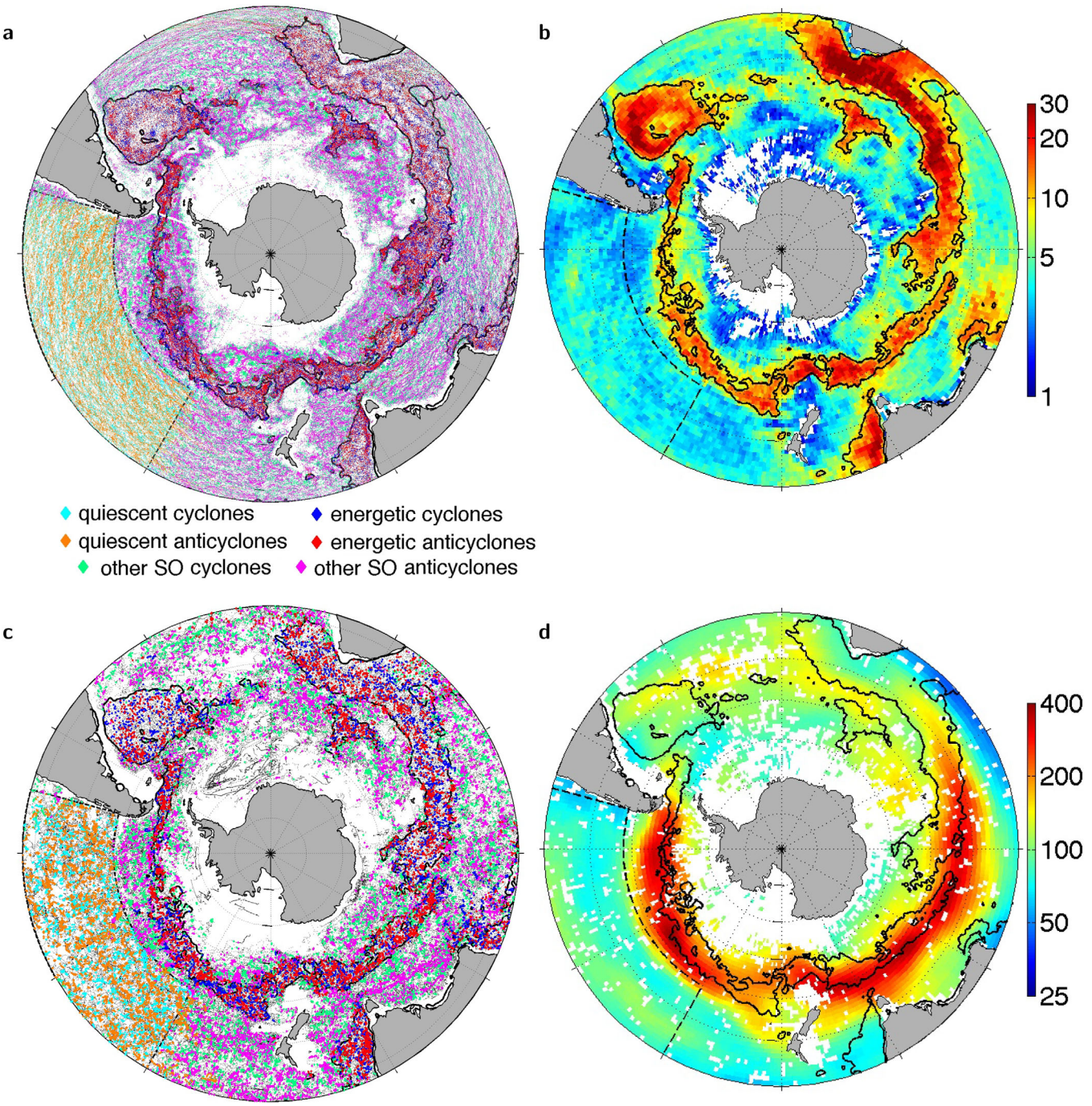

Figure 1. SO eddy and Argo data coverage and climatologies. (a) Locations of cyclonic and anticyclonic eddy instances (each dot indicates a weekly eddy snapshot), color coded as indicated in the legend by region of eddy track origin: in the South Pacific quiescent region (dashed box), in the SO energetic regions (solid contours), or elsewhere in the SO. (b) Corresponding SO eddy amplitude in sea surface height (cm), estimated as average over 1°-by-1° bins (here for the 12 year period 2000–2011, white if no eddy coverage). (c) Locations of Argo profiles, in small black markers if outside eddy cores, color coded as in Figure 1a if inside eddy cores. (d) Corresponding Argo profile mixed-layer depth climatology $\bar{h}$ (m) in late winter (August-September-October, ASO)—mapped, as detailed in supporting information Note S2, using cluster averaging to a 1°-by-1° grid over the Argo covered region (white elsewhere).

(see supporting information Figure S1 for a schematic). The resulting spatial and temporal scales resolved in this Argo profile seasonal mixed-layer depth climatology are typically 200 km and 15 days (cf. supporting information Figure S2 and Note S1). The underlying seasonal profile locations are mapped in supporting information Figure S3, with their census provided in Table 1. For reference, the resulting climatology for late

Table 1. Southern Ocean Data Coverage[a]

	Quiescent			Energetic			SO $\leq$ 27.5°S		
n_s	104,762	26,800	26,963	177,045	45,764	45,109	743,905	187,914	194,423
$\frac{n_sC}{n_sA}$	0.82	0.85	0.80	1.02	1.02	1.02	1.02	1.02	1.01
n_p	36,685	8832	9563	43,132	10,184	11,187	202,401	47,755	53,926
$n_{ps\,core}$	7113	1688	1936	9536	2124	2557	35,295	8374	9269
$\frac{n_{ps\,core}C}{n_{ps\,core}A}$	0.78	0.77	0.74	0.95	0.92	0.95	0.97	0.95	0.93

[a]Number of weekly eddy snapshots n_s (including both cyclones C and anticylones A, with their ratio $\frac{n_sC}{n_sA}$ indicated in italics below), number of Argo profiles n_p, and number of Argo-profile associations with snapshots of (0.75 r_e) eddy cores $n_{ps\,core}$. Based on August 2001–March 2012 data. Each three-part entry shows a value including all months of the year, followed by that for late winter months (August-September-October), and the summer time (January-February-March).

winter, i.e., including $\bar{h}$ of all profiles collected in August, September, and October (ASO), is mapped in Figure 1d. The method used here to map individual Argo profile data is detailed in supporting information Note S2, with mapping scales displayed in supporting information Figure S4. In agreement with previous climatologies [e.g., *Dong et al*., 2008], the mapped winter climatology (Figure 1d) shows deep winter mixed layers, typically in excess of 100 m, locally exceeding 400 m along and equatorward of the ACC energetic regions. The annual-mean climatology reveals an overall similar spatial pattern, with a secondary broader peak along and poleward of the ACC reflecting the summer-time wind-driven mixed-layer depth maximum of $\approx$ 70 m there (see supporting information Figure S1). Starting at the end of summer, SO $\bar{h}$ deepen slowly to peak in August and September, followed by a rapid re-stratification toward the summer-time (January-February-March, JFM) minimum (not shown—see also, e.g., *Dong et al*. [2008] and *Sallée et al*. [2010b] for a discussion of the SO mixed-layer depth climatology).

3. Characterizing the Eddy Signal in Mixed-Layer Depth

Individual Argo profile mixed-layer depth climatologies $\bar{h}$ and anomalies h' are now used in combination with the eddy data set to provide a systematic assessment of eddy-induced variability in mixed-layer depth across the SO.

3.1. Mixed-Layer Depth Variability and a Systematic Eddy Signal

Figure 2 (black curve) displays the distribution of mixed-layer depth anomalies h' over all SO Argo profiles in the $10\frac{2}{3}$ analysis period from the start of the Argo era in the SO (August 2001) up to the end of the eddy data set (4 April 2012). The departures h' from the seasonal climatology of mixed-layer depth at the profile locations in time and space are seen to have a typical magnitude of $\approx$ 40 m. They reflect nonseasonal mixed-layer depth variability at all spatial scales and at time scales up to several years. Positive (deep) mixed-layer depth anomalies are observed to occur at a somewhat larger frequency and magnitude than negative (shallow) anomalies. Moreover, observed h' distributions are peaky, that is small amplitude variability in mixed-layer depth ($\leq 1\sigma$) and excursions of large magnitude ($>3\sigma$) are more frequent, and typical amplitude variability ($1-3\sigma$) less frequent, than expected for normally distributed signals of equal mean and standard deviation (see black dashed curve).

To assess the signatures of the oceanic mesoscale in this observed variability in SO mixed-layer depth, Argo profiles are collocated with occurrences of mesoscale eddy snapshots, resulting in a data set of profile-to-snapshot distances in time δt_{sp} and space r_{sp}. Profiles are associated to eddy snapshots if collected within the same week as the altimetry snapshot ($|\delta t_{sp}| \leq 4$ days) and collocated to neighboring eddy centers as a function of their normalized radial distance (r_{sp}, normalized by the radius of the eddy snapshot r_e). A summary schematic of the various scales involved is provided in supporting information Figure S1.

Table 2. Southern Ocean Eddy Statistics[a]

	Quiescent	Energetic	SO $\leq$ 30°S
r_e (km)	80	82	72
$\lvert A_e \rvert$ (cm)	3.5	15.2	6.6
f_E	0.16	0.18	0.12
$\frac{f_E}{1-f_E}$	0.19	0.23	0.13

[a]Eddy radius r_e, eddy amplitude $|A_e|$, and the time-average fraction of area covered by eddy cores f_E (estimated as in Figure 6c), for the Southern Ocean and its quiescent and energetic regions (as introduced in section 2, see Figure 1).

We first focus on variability within mesoscale eddy cores, defined to extend out to ≤ 0.75 eddy radii from the eddy centers. As will

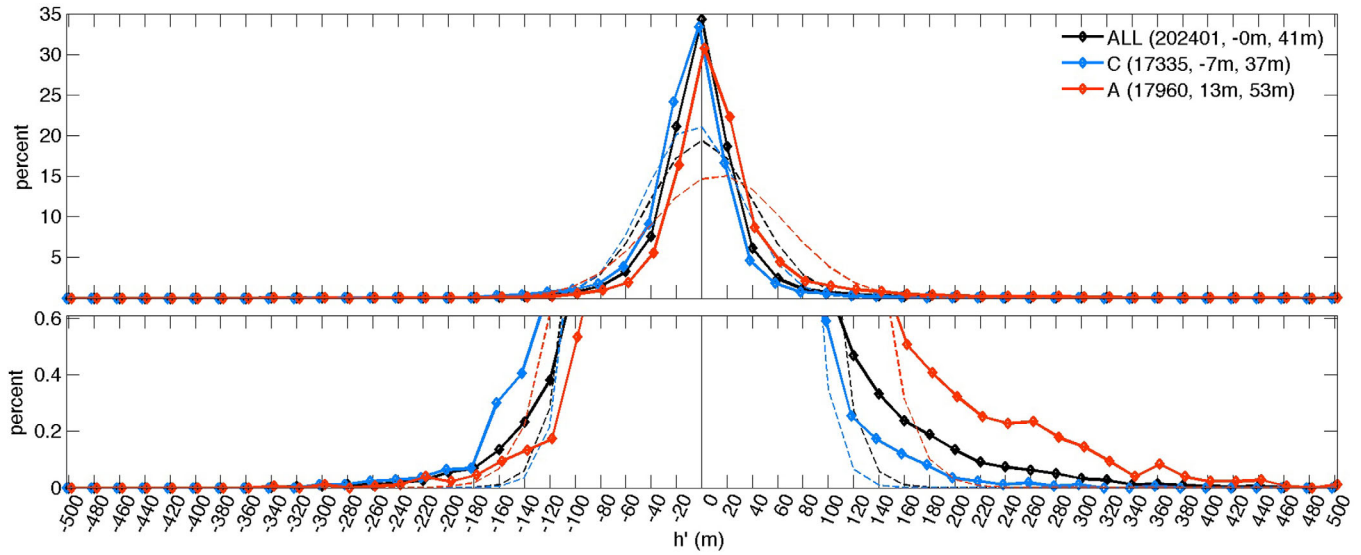

Figure 2. Probability distribution of anomalies in mixed-layer depth, h', across all Argo profiles in the Southern Ocean south of 27.5°S (black), and only those profiles located within the cores of anticyclonic (red) and cyclonic eddy snapshots (blue). Profile numbers, mean and standard deviation of the h' distribution are indicated in the inset legend, and the corresponding normal distributions are shown by dashed curves.

become clear, this choice balances trade-offs between the observational sample number available within such defined cores and the amplitude of the detectable eddy signal. To assess eddy-core mixed-layer depth signals, we single out instances in which profiles are collected where and when such identified SO eddy cores are present (i.e., $\frac{r_{sp}}{r_e} \leq 0.75$ and $|\delta t_{sp}| \leq 4$ days). This is the case for roughly 15% of the SO Argo profiles collected during the analysis period, resulting in a data set of more than 35,000 eddy-core profile associations, with roughly equal sampling of cyclones and anticyclones (Table 1). Profiles coincide with eddy cores wherever eddies are present across the SO (Figure 1a versus colored dots in Figure 1c). They sample the cores of about 5% of the identified weekly SO eddy snapshots (Table 1). Of these Argo-sampled eddy core snapshots, most are sampled by a single profile (about 94%), slightly more than 5% are sampled by two, and about 0.5% by more than two profiles (not shown). Note that roughly 10% of the identified profile-eddy core snapshot associations consist of a given profile being associated with two eddy cores. In more than 99% of these cases, these are the cores of the same eddy in two consecutive weekly snapshots along its track. This reflects slow eddy propagation timescales and the choice of a 4 day threshold in δt_{sp}, which allows for a slight overlap between weeks.

The distributions of Argo profile mixed-layer depth anomalies across the cores of sampled cyclonic and anticyclonic eddy snapshots (blue and red curves in Figure 2) reveal the presence of deep and shallow excursions of mixed-layer depth from the background seasonal climatology, with probability distributions similar in shape to that seen when drawing from all profiles irrespective of their location with respect to eddies (black curve). Yet anomalously deep mixed-layer depth events (positive h') are encountered more frequently when sampling only anticyclonic eddy cores (red curve) than when sampling all profiles irrespective of their association to eddy cores (black curve). Conversely, the probability of encountering shallower than climatological mixed layers is enhanced when sampling only cyclonic eddy cores (blue). In particular, the probability of encountering anomalously deepest mixed layers is substantially larger when drawing only from anticyclonic cores, compared to sampling anywhere, and even more so compared to drawing only from cyclonic cores. These systematic differences in probability reflect: (1) differences in the skewness (the anticyclonic core h' distribution is more skewed toward large positive h' than the all-profile distribution, whereas the cyclonic h' distribution is almost symmetrical with a small negative skewness), and (2) a systematic shift of the means of the distributions (toward positive/negative h' within anticyclonic/cyclonic eddy cores). Note that the large variability of h', which reflects eddy-to-eddy differences as well as non-eddy processes, is present when sampling all Argo profiles as well as cyclonic or anticyclonic eddy cores alone. Excursions of both signs, deep or shallow, are thus regularly encountered within eddy cores of either polarity. Interestingly, the variance of h' is somewhat enhanced in anticyclones (standard deviation larger

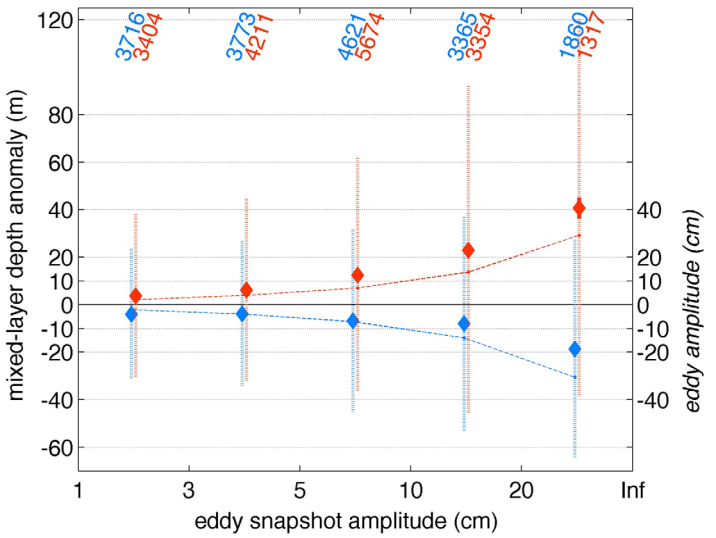

Figure 3. SO eddy-core composite mixed-layer depth anomaly h' (diamonds, in m) for cyclones (blue) and anticyclones (red), as a function of the eddy-snapshot sea surface height amplitude (increasing along the horizontal axis. The composite averages of eddy amplitudes by bin are displayed by the dashed lines, in cm). Thick vertical lines indicate a 95% confidence interval on the composite average h' (note these are often as narrow as the symbol size and thus not visible), dotted lines a ± 1 standard deviation interval. Numbers composited are indicated at the top.

than in the "all-profile case" by $\approx$ 10 m), and reduced in cyclones (smaller by $\approx$ 5 m, see figure legend). This suggests a possible contribution of mesoscale eddies to variability in mixed-layer depth in the SO, which is further explored in the discussion section.

Composite averaging over a large number of eddy snapshot-profile associations is now used to isolate, and further characterize, any systematic average eddy signal within the observed variability in h'. The composite-average eddy-core mixed-layer depth anomalies h' across all SO eddies are given by the means of the distributions in Figure 2. They amount to a shallow anomaly of -7 m over cyclones, and a more pronounced deep anomaly of $+13$ m over anticyclones. These both lie well outside the 95% range on the mean h' expected for samples of the given size drawn from a population with the observed variance and a true zero mean (which are ± 0.6 m for cyclones, and ± 0.8 m for anticyclones), and contrast with a mean h' of 0 ± 0.2 m for the all profile distribution (black curve). The composite-average eddy-core h' over cyclones and anticyclones thus reflect systematic, statistically significant, average eddy perturbations in SO mixed-layer depth.

One would like to know how these eddy signals in mixed-layer depth depend on the amplitude of the eddying circulations themselves. To assess this, the distributions of Argo profile h' are reevaluated sampling only the cores of eddy snapshots whose amplitude in sea surface height A_e fall within a given range. From the weakest quartile of SO eddy snapshots with amplitudes of $1-3$ cm, to the most intense eddies with amplitudes in excess of 20 cm ($\approx$ 6% of SO eddy snapshots), the result (Figure 3) reveals large h' variability that embeds anomalously deep composite-average h' within anticyclonic eddy cores and anomalously shallow h' of weaker magnitude within cyclonic eddy cores. These eddy signals in mixed-layer depth differ significantly from zero across all bins of A_e considered, and show a systematic increase with eddy amplitude. Eddy $|h'|$ increases by typically 1 m for each 1 cm increase in the eddy amplitude $|A_e|$. Notably anticyclonic h' increase at a slightly higher, and cyclonic h' at a slightly lower rate. This leads to a systematic asymmetry toward larger-magnitude eddy signatures in surface mixed-layer depth over anticyclones for all eddy intensities, whereas eddy amplitudes (dashed curves) themselves are symmetrical in magnitude between cyclones and anticyclones in each of the amplitude bins. Eddy core h' signals (markers) thus amount to roughly $+20$ m versus -10 m over anticyclones versus cyclones in the $10-20$ cm amplitude range, and increase in magnitude to roughly $+40$ m versus -20 m in the composite over eddies with amplitudes larger than 20 cm. Interestingly, the level of h' variability (dotted vertical lines) around these systematic average eddy signals is also systematically elevated over anticyclones compared to cyclones, and also increases with increasing eddy amplitude: from typically 30 m over the weakest eddies, to 50 m over the most intense cyclones versus to $\approx$ 80 m over the most intense anticyclones.

To get an idea of the spatial variation of eddy h' across a typical eddy, the composite eddy signals are now diagnosed, rather than in the average across eddy cores, in bins of normalized radial distance (r_{sp} normalized by the eddy radius r_e) from eddy centers. To capture some of the variations with eddy amplitude and across the SO in this analysis, while still retaining a large enough sample to isolate robust eddy signals from the variability, here we focus on snapshots of eddies whose tracks originate in either the SO quiescent or

energetic regions (see black contours in Figure 1a, with the locations of the corresponding eddy snapshots color coded). The result (Figure 4a) reveals eddy signatures in mixed-layer depth that peak at the eddy centers, at a modest +7 m versus −4 m in the composite over quiescent regions' anticyclones versus cyclones (orange versus cyan), and at +45 m versus −15 m over SO energetic region eddies. Moving out from the eddy center (in increments of 0.25 eddy radii), eddy h' decay in magnitude, remaining statistically nonzero (at 95% confidence) all the way up to a distance of one eddy radius. The decay of h' observed moving out from the eddy centers may also in part result from the decreasing probability of being within an eddy core that arises in the presence of noncircular eddy shapes. Note the radii provided in the eddy track data set are determined to delimit circles of only area equal to that covered by the actual eddy shapes—see CSS11. Based on these results, the eddy cores have been defined to extend outward to 0.75 eddy radii, i.e., across the region where the largest signal resides.

Figure 4a also reveals a systematic lobe of reversed sign in the h' composites centered at around two eddy radii. Such lobes are also seen surrounding eddy cores in the SO eddy SST signatures [*Hausmann and Czaja*, 2012], and likely reflect the dense packing of eddies in the SO (and a statistical average distance to neighboring eddy cores of mostly opposing polarity). Beyond about 3.5 eddy radii, composite-average h' are statistically undistinguishable from zero. This suggests a non-periodic nature of the SO eddy field (with an essentially random probability of encountering, or not, eddy cores of either polarity beyond the respectively neighboring eddy of statistically opposing polarity). The zero average h' outside the zone of eddy influence also attest to the capacity of the available sampling and method to detect robust eddy signals that are uncontaminated by residuals of the large (non-eddy) h' variability.

Note that for each of the four ensembles investigated in Figure 4a, the number of h' observations composited rises with increasing radius (along the horizontal axis) as expected from the increase in area of radial rings, from $\approx$ 500 at the eddy centers to more than 10,000 for bins beyond about 3 eddy radii. These changing sample numbers are accounted for in the assessment of statistical significance of the composites in each of the radial bins. (See supporting information Figure S5 and Note S3 for additional discussion of the statistics underlying Figure 4). The results presented in Figures (2 and 3), and 4a are based on density-threshold-identified mixed-layer depths. Above overall conclusions remain robust when instead using mixed-layer depths h obtained with the density algorithm developed by *Holte and Talley* [2009, cf. section 2] (The latter result in overall slightly shallower SO climatological mixed-layer depths and somewhat smaller-magnitude composite eddy h' anomalies, see supporting information Note S3 and Figure S5).

3.2. Characterizing the Seasonality of the Eddy Mixed-Layer Depth Signal

The large seasonality in SO climatological mixed-layer depths (see section 2) poses the question whether eddy signatures therein also vary throughout the year, due to either seasonal variations in the SO eddy field itself or seasonality in the way eddying circulations perturb mixed-layer depth, which may depend on the background seasonal state. The eddy mixed-layer depth signals presented above reflect observations, profiles, and eddy snapshots, collected throughout the analysis period, including all months of the year. Data coverage and the occurrence of identified eddy snapshots show little systematic seasonal variation (Table 1, see also supporting information Figure S3 for seasonal maps of eddy snapshot and Argo profile locations, equivalent to those shown for year-round data in Figures 1a and 1c.) The above results (Figures (2 and 3), and 4a) thus closely reflect an annual-mean eddy signal in SO mixed-layer depths. Now to assess whether eddy signatures in SO surface mixed-layer depth show a seasonal modulation, composite average h' are diagnosed only including snapshots of eddies detected and sampled by Argo profiles in each month of the year.

First, we look at h' signatures within eddy cores. For each of the four groups considered here (energetic and quiescent regions cyclones and anticyclones) between 200–500 eddy-core, Argo profiles are available to composite in each month of the year (see supporting information Figure S5). These Argo-sampled eddy cores, as discussed above for year-round data, represent a small fraction of the total number of eddies detected by the eddy-identification algorithm, and this fraction is also relatively constant throughout the year (not shown). The resulting eddy-core h' composite averages by month of year (Figure 4b) reveal a clear seasonal modulation of the eddy signal in mixed-layer depth (note that these represent departures from the seasonal climatology). The seasonal variation in the magnitude of the eddy signal $|h'|$ broadly follows that of the background seasonal state $\bar{h}$: it is characterized by weak eddy perturbations to the shallow

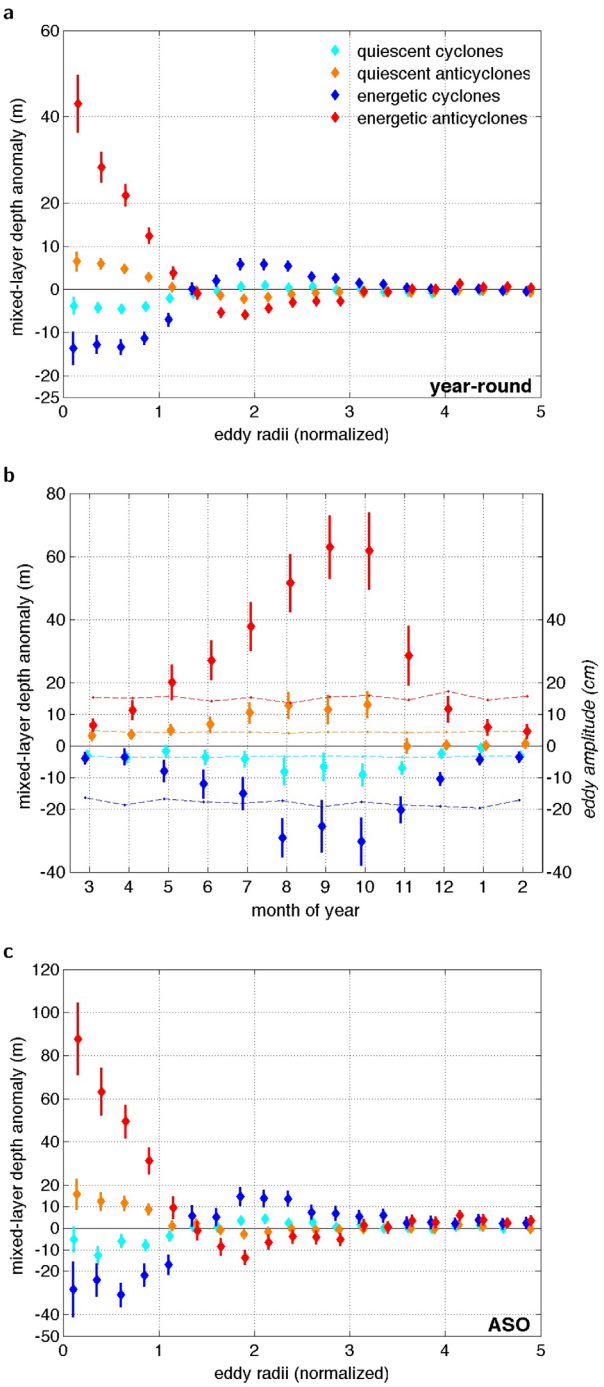

Figure 4. SO quiescent and energetic region eddy mixed-layer depth signatures, and their seasonal evolution. Mixed-layer depth anomaly h', in m: (a) composite-averaged across Argo profiles as a function of their distance from the center of cyclonic and anticyclonic eddies with origins in the South Pacific quiescent region (cyan and orange) and the SO energetic regions (blue and red)—see Figure 1b for a map of these regions. The number of profiles composited in the inner-most radius bin ($\leq$0.25 eddy radii) of cyclones and anticyclones are 371 and 455 in the quiescent, and 522 and 546 in the energetic regions—numbers increase outward as expected from the increase in area (see supporting information Figure S5). Thick lines indicate a 95% confidence interval on the composite means (note these are often as narrow as the symbol size and thus not visible). (b) composite-averaged across profiles within eddy cores ($\leq$0.75 eddy radii) as a function of season (month of year is indicated along the horizontal axis). For each month of the year, typically 400 Argo profiles are composited, for both cyclones and anticyclones, and in each of the regions considered. Color-coding as in Figure 4a. Dashed lines indicate the composite-average eddy sea surface height amplitude, in cm. (c) as in Figure 4a, but only including the late winter months (August-September-October, ASO), during which the eddy h' signatures are most intense.

summer mixed layer and intense eddy perturbations to the deep winter mixed layer. In quiescent regions, the eddy signals are weak throughout the summer months (anticyclonic composites are not statistically different from zero from November through February, cyclonic composites loose significance in January and May). Systematic quiescent eddy-core h' signatures emerge later in the fall and increase in magnitude through to the late winter (August-September-October, ASO in the following), when they peak at a 12 ± 4 m deep anomaly within anticyclones versus an 8 ± 4 m shallow anomaly in cyclones. Within eddies with origins in SO energetic regions, eddy-core h' are significant, being deep in anticyclones versus less pronounced and shallow in cyclones, throughout the year. Here eddy-core signals are weakest in January-February-March (JFM) at 6 ± 2 m versus -4 ± 2 m, and peak in late winter (ASO) at 59 ± 10 m versus -28 ± 7 m.

In contrast to this systematic and pronounced seasonal modulation of eddy-core signatures in SO mixed-layer depth, eddying circulations themselves do not vary seasonally in amplitude (dashed lines Figure 4b). Thus, eddy circulations of a given amplitude perturb mixed-layer depth more vigorously in winter when background mixed layers are deep. Asymmetries in magnitude between anticyclonic and cyclonic h' signals are also largest in late fall through late winter (with a ratio $\frac{h'_A}{-h'_C}$ of typically 2–3), and become more symmetric in the summer. Interestingly, the eddy signal peaks at the end of winter (October) when the background climatological mixed layer has begun to shoal (supporting information Figure S5). Expressed as fraction of $\bar{h}$, energetic regions' eddy signals are about $\frac{1}{10}$ in magnitude in the summer time, and rise during the fall, to reach nearly $\frac{1}{2}$ over anticyclones, and $-\frac{1}{4}$ over cyclones, at the end of winter (not shown).

Possible physical mechanisms underlying the peak of the eddy mixed-layer depth signal at the end of winter may involve penetration of the base of the deep climatological mixed layers in winter to depths where eddy-induced isopycnal displacements are larger, thus causing larger perturbations to the background stratification on which mixing processes operate (see, e.g., vertical sections in *Frenger et al.* [2015]). The more pronounced eddy perturbations to sea surface temperature, and thus air-sea heat loss and associated mixing, in the winter time may also play a role [see, e.g., *Hausmann and Czaja*, 2012; *Frenger et al.*, 2013]. In the following, we characterize this large winter signal in more detail, focusing on late winter months (ASO) when the eddy signatures in mixed-layer depth peak in magnitude. The evolution moving outward from the eddy centers (displayed in Figure 4c) shows a similar pattern as that seen in year-round observations (Figure 4a), with a peak at almost $+90$ m in energetic anticyclonic eddy centers.

To examine geographical variations of the eddy-core h' signal in winter, we first assess the resolution at which this is possible. At a sample number of 1000, typical for the ensemble of profile associations to eddy cores during ASO in each of the four eddy groups considered (supporting information Figure S5), the standard error on eddy-core composite averages is about 1 m over quiescent eddies ($\sigma \approx 25$ m), 2 m over energetic cyclones ($\sigma \approx 70$ m), and 3 m over energetic anticyclones ($\sigma \approx 100$ m). For truly zero eddy signals, there is thus a 95% probability to encounter composite averages with a magnitude as large as 2, 4, and 6 m, respectively. As the sample numbers are reduced, the magnitude of such chance-encountered nonzero composite averages increases. At a sample number of 50, they amount to $\approx$ 10, 20, and 29 m. This corresponds to a magnitude that is comparable to the eddy-core h' signal for quiescent eddies in ASO ($\approx \pm 10$ m, Figure 4b), and lies at $\frac{2}{3}$ and $\frac{1}{2}$ of the magnitude of the eddy signal for energetic cyclones (-30 m) and anticyclones ($+60$ m). This suggests we can take a more stratified look at ASO eddy-core signatures by composite averaging over samples of as little as 50 members.

The eddy signal is now mapped using this threshold sample size. To do so, for each 1°-by-1° grid box, a composite average h' is diagnosed over this fixed number of $N_{map} = 50$ surrounding Argo profile eddy-core associations identified as closest in terms of a mapping cost function (see supporting information Note S2 for details on the mapping procedure and its statistics). The resulting average mapping radii for both cyclonic and anticyclonic eddy-core signals amount to typically 500 km, varying between 300 and 1000 km in the SO away from sea ice and continental shelves (supporting information Figure S4). In the resulting maps of the winter-time, eddy-core anomaly in mixed-layer depth (Figure 5) stippling indicates where mapping radii exceed 700 km within the Argo-covered region. The maps reveal deep eddy-core h' in anticyclones over the entire SO (Figure 5b), and predominately shallow eddy-core h' over cyclones (Figure 5a). The latter map suggests a few exceptions with deep eddy-core h' over cyclones located mainly to the south and southwest of Australia. (These correspond to the "sub-thermocline" cyclones featuring warm sea surface temperature anomalies and depression of near-surface isopycnals as characterized by *Frenger et al.*

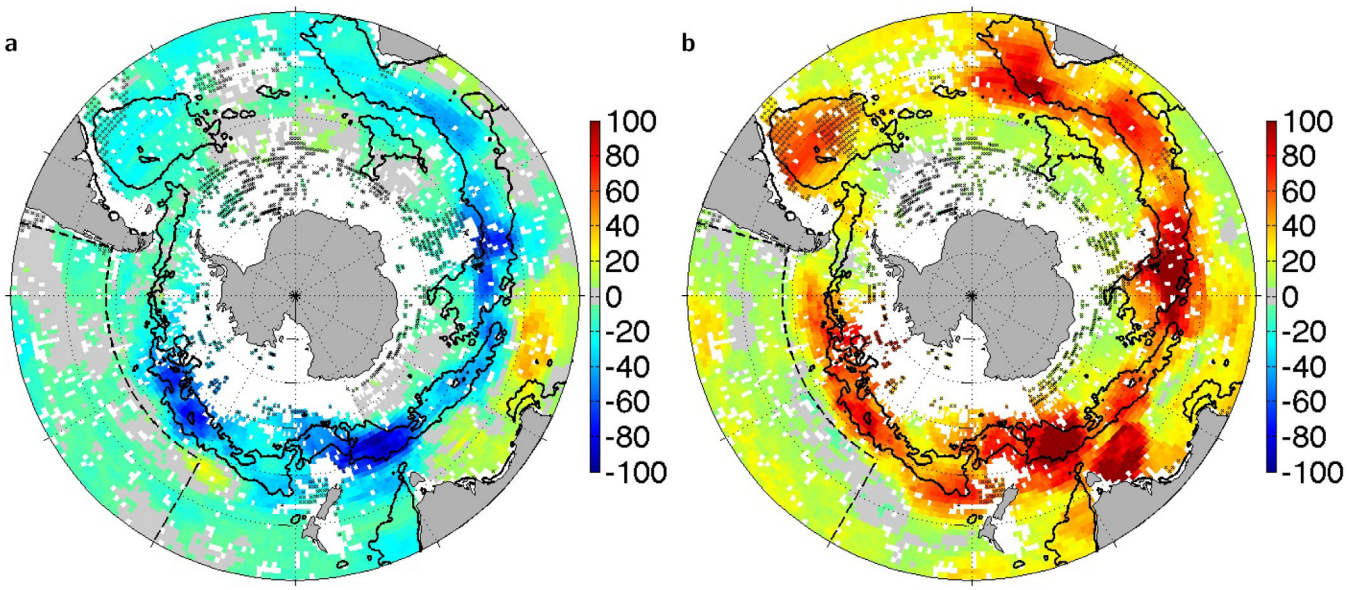

Figure 5. Maps of the SO eddy-core mixed-layer depth signals in winter (August-September-October), estimated, as detailed in supporting information Note S2, using cluster averaging over 50 nearest profiles within (a) cyclonic and (b) anticyclonic eddy cores ($\leq$0.75 eddy radii), onto a 1°-by-1° grid over the Argo-covered region (in white-shaded grid boxes no Argo profile, be it within or outside an eddy core, is collected during ASO). Regions in which the resulting mapping radius r_{map} (see supporting information Figure S4) exceeds 700 km are stippled. Black contours as in Figure 1.

[2015, supporting information Figure S9]. Note that excluding this group of cyclones results in slightly shallower mixed-layer depth anomalies in the remaining SO energetic region cyclonic composite average, e.g., in Figure 4—not shown.) Overall, the maps in Figure 5 suggest a spatial pattern, similar for cyclones and anticyclones, of weak magnitude eddy perturbations to winter mixed-layer depth in the subtropical basin gyre interiors, and increasing magnitudes on approaching the regions of high eddy energy along the ACC, the Agulhas retroflection, the Agulhas return current, and also the Brazil-Malvinas confluence. This suggests the separation into quiescent and energetic region eddies used above is a meaningful one that reflects the primary large-scale spatial pattern in SO eddy mixed-layer depth signatures. Summer-time maps (JFM, not shown) feature much weaker amplitude signatures throughout the SO. Maps of the year-round eddy signal, which are better resolved due to a roughly four times larger sample size, show a similar spatial pattern to the winter signal displayed and discussed here.

4. Discussion

This section probes some of the implications of the observed systematic eddy h' signatures for the mean state of the SO mixed-layer depth field, in terms of its climatological mean, level of variability, and deepest winter excursions.

4.1. Do Eddies Have a Rectified Impact on the SO Mean State in Mixed-Layer Depth?

Observational results show that anticyclones deepen the SO mixed layer by more than cyclones shallow it. This systematic asymmetry in the magnitude of eddy-induced perturbations poses the question whether mesoscale eddies have a rectified impact on the mean state of the SO mixed-layer depth field. The observed asymmetry is more pronounced in the winter time and along the ACC energetic regions, suggesting that in the absence of eddies the winter mixed layers along the ACC might be shallower.

As a first step toward assessing whether this is the case, the composite h' signature of all SO eddies are examined by including both cyclones and anticyclones in the averages, denoted $\langle h'_E \rangle$ in the following (where $\langle\rangle$ stands for composite average, E for eddy). Maps of these all eddy-core composites $\langle h'_E \rangle$ in late winter (ASO, Figure 6a) indeed show a net deep eddy mixed-layer depth anomaly across most of the SO. The net eddy signal $\langle h'_E \rangle$ is weak in quiescent gyre interiors, only occasionally exceeding 10 m. In several parts of the energetic regions and to the south and south-west of Australia, $\langle h'_E \rangle$ increases to 20–50 m. Note

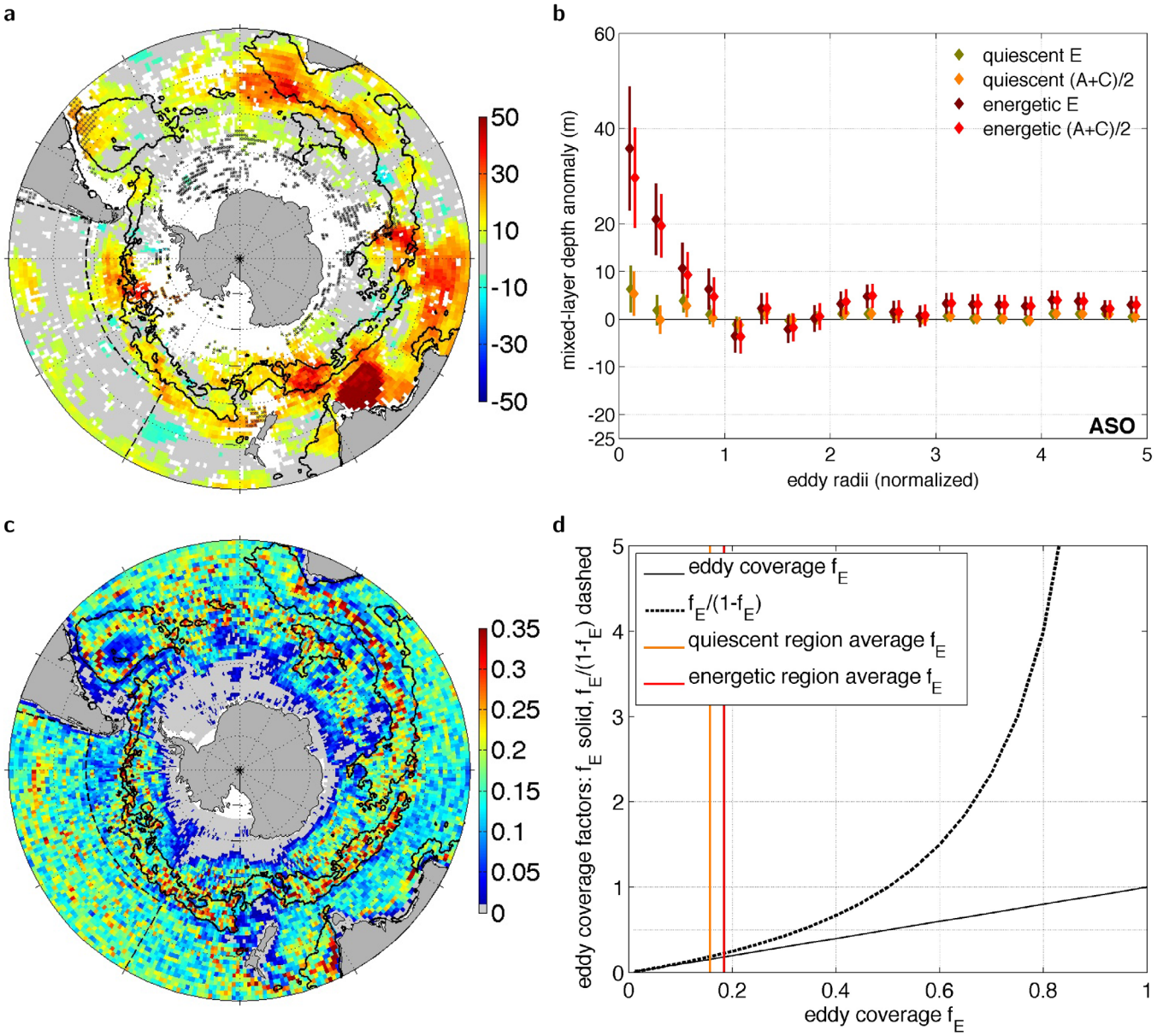

Figure 6. Net winter-time eddy mixed-layer depth signal. (a) Map of the net eddy-core late-winter (ASO) mixed-layer depth anomaly, including both cyclones and anticyclones. Otherwise as in Figure 5. (b) As in Figure 4c, but with composites including both cyclones and anticyclones (denoted *E*), compared to the average of the anticyclonic and cyclonic eddy composites (denoted $(A+C)/2$). (c) Time-average area coverage fraction by eddy cores (within 0.75 r_e), denoted f_E and estimated as average over 2°-longitude by 1°-latitude bins, based on the 12 year period 2000–2011. (d) Illustration of the sensitivity of eddy rectification, as estimated from observed eddy anomalies, to eddy coverage (see text).

that, compared to the maps in Figure 5, the sample size entering the composite at each grid point in Figure 6a is doubled (by specifying $N_{map} = 100$ and thus conserving roughly equal mapping scales to those of the cyclonic or anticyclonic h' maps—see supporting information Note S2 and Figure S4). The magnitude of the signal is however reduced by more than half due to the averaging of opposite sign cyclonic and anticyclonic h', thus leading to somewhat reduced statistical significance in Figure 6a. The composite radial structure of the net eddy $\langle h'_E \rangle$, in ASO, evaluated over all quiescent and energetic eddies (Figure 6b, displayed in the same format as in Figure 4c) is weak over quiescent eddies, and peaks at a statistically significant average of $\approx +5$ m at the eddy centers (in the bin of 0.25–0.5 eddy radii the quiescent eddy signal straddles the limit of being significantly different from zero). In the average over energetic eddies, $\langle h'_E \rangle$ is significantly positive all the way out to one eddy radius, and peaks at $\approx +35$ m at eddy centers. Correction for a small bias in the Argo profile sampling of eddy cores (preferential sampling of anticyclones compared to eddy statistics

inferred from satellite altimetry, see Table 1) leads to a slightly smaller peak $\langle h'_E \rangle$, reduced by $\approx$ 3 m over energetic region eddy centers (not shown). Note that the all-eddy composites $\langle h'_E \rangle$ are very similar to the average of anticyclonic $\langle h'_A \rangle$ and cyclonic $\langle h'_C \rangle$ composite signals evaluated individually (separate set of markers in Figure 6b, see legend), i.e., $\langle h'_E \rangle \approx (\langle h'_A \rangle + \langle h'_C \rangle)/2$, in both the quiescent and energetic region averages. Locally, and especially along the edges of the ACC energetic regions, observed asymmetries in cyclonic and anticyclonic eddy demographics [see, e.g., *Frenger et al*., 2015, Figure 6b] additionally contribute to setting the observed spatial patterns of $\langle h'_E \rangle$ in Figure 6a (not shown).

To evaluate the degree to which these net eddy mixed-layer depth anomalies $\langle h'_E \rangle$ contribute to the mean-state in SO winter mixed-layer depth, the fraction of time and space occupied by eddies needs to be taken into account. The coverage fraction by eddy cores, denoted f_E, is mapped in Figure 6c. It is estimated as an average over 2°-longitude by 1°-latitude bins. Given the large eddy snapshot sample numbers bin-averaging without smoothing is used here, thus the patchiness of the map. The fraction varies from less than 5% on continental shelves and adjacent to Antarctic sea ice, increasing to slightly more than 15% in the average over the South Pacific quiescent regions and slightly less than 20% on average over the energetic regions (Table 2), to values in excess of 30% reached locally along the ACC (Figure 6c). Notably, f_E shows little seasonal variation, so that winter and summer time maps are similar to the annual mean displayed here (not shown).

If the climatology $\bar{h}$, to which h' and eddy-averages therein are referenced, would reflect a mean state from which eddies are absent, the rectified eddy contribution, denoted $\delta\bar{h}$ hereafter, could be estimated observationally as $f_E\langle h'_E \rangle$. However, this is not the case, because the observed mean state already includes any rectified eddy contribution if it exists, i.e.,

$$\bar{h} = \bar{h}^u + \delta\bar{h}. \tag{2}$$

Here $\bar{h}^u$ denotes the unperturbed climatological mean state of the SO, which would exist in the absence of eddies and is thus not observable. One approach to estimating $\delta\bar{h}$ observationally begins with decomposing h into the observed mean state, $\bar{h}$, and departures from this state, h', and relate these to $h'u$, the departures from $\bar{h}^u$ that are not accessible observationally, by applying equation (2):

$$h = \bar{h} + h' = \bar{h}^u + (\delta\bar{h} + h') \equiv \bar{h}^u + h'u. \tag{3}$$

Using equations (2) and (3), one obtains an expression for the rectified eddy contribution only in terms of observable quantities, as follows:

$$\begin{aligned} \delta\bar{h} &= f_E\langle h'^u_E \rangle = f_E\left(\langle h'_E \rangle + \delta\bar{h}\right) \\ &= \frac{f_E}{1-f_E}\,\langle h'_E \rangle. \end{aligned} \tag{4}$$

Rectification and its observational estimate are thus highly sensitive to f_E (Figure 6d). If $f_E = 0$, there are no eddies, and no rectification. If eddy cores occupy all the area 100% of the time, f_E equals 1 and the perturbed mean state is completely determined by eddies (note however that this is physically impossible, especially with the 0.75 r_e cutoff for eddy cores considered here). In this scenario, any asymmetry in eddy anomalies with respect to the unperturbed state, $\langle h'^u_E \rangle$, is fully absorbed into the perturbed state, and is thus cancelled out if evaluated with respect to the perturbed state. Rectification is thus not observable at $f_E = 1$ (i.e., from equation (4), $\langle h'_E \rangle$ is unrelated to $\delta\bar{h}$). If $f_E = 0.5$ rectification is given directly by the net eddy signal in mixed-layer depth $\langle h'_E \rangle$. For $f_E \ll 1$, as observed (Figure 6c), $\frac{f_E}{1-f_E} \approx f_E$ and thus $\delta\bar{h} \approx f_E\langle h'_E \rangle$. In quiescent regions, this is about 0.16×2 m < 0.5 m, over energetic ACC regions it amounts to on average 0.18×15 m ≈ 3 m. Note that these estimates are not anticipated to be very sensitive to the definition of eddy cores, as when larger radius thresholds are chosen to delimit cores, f_E increases while the average eddy-core $\langle h'_E \rangle$ decreases. This analysis thereby suggests that the contribution of mesoscale eddies to the climatological mean depth of the SO mixed-layer depth field is small. That is, in late winter and in the ACC energetic regions, when and where the eddy effect peaks, it amounts to a deepening of the mean state mixed-layer depth by about 3 m in 150 m, or 2%. This, for example, corresponds to a 2% ($\approx$ 10 day) increase in the typical time scale for turbulent air-sea heat exchange in this region and season, $\tau = \frac{\rho c_p h}{\alpha} \approx 15$ months, where ρc_p is the specific heat of seawater per unit volume and α is the turbulent air-sea heat flux feedback,

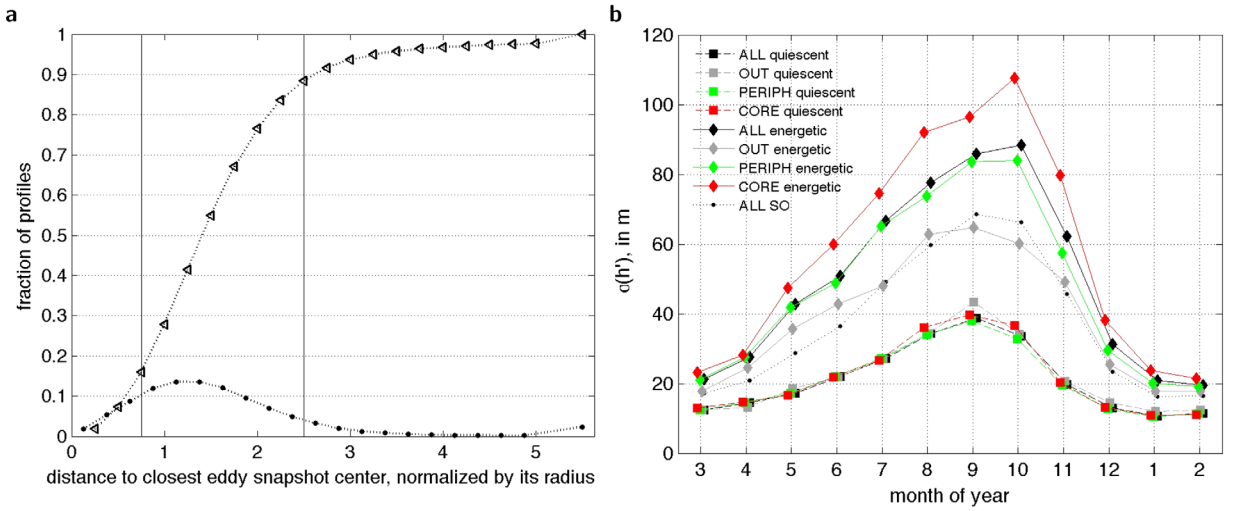

Figure 7. Eddy contribution to SO h' variability and its seasonal modulation. (a) Distribution (dots), and cumulative distribution (triangles), of the distance of SO Argo profiles to the center of the closest eddy snapshot identified within the same week ($|\delta t_{sp}| \leq 4$ days), expressed as fraction of all profiles (vertical axis). Distances are normalized by the radius of the closest eddy snapshot $\frac{r_{sp}}{r_e}$ (horizontal axis), and vertical lines indicate normalized distances corresponding to the chosen limits of eddy cores (at $\frac{r_{sp}}{r_e}=0.75$) and eddy peripheries (out to $\frac{r_{sp}}{r_e}=2.5$). The last distance bin includes all profiles for which the closest eddy center in the same week lies at $\frac{r_{sp}}{r_e} > 5$. (b) Mixed-layer depth variability as a function of season (horizontal axis), measured by the h' standard deviation (vertical axis, in m) evaluated: across all Argo profiles (black, ALL), over only those profiles within the cores of either cyclones or anticyclones (red, CORE), those profiles not within eddy cores but within their periphery (green, PERIPH), and the remainder of profiles further out from the closest eddy snapshot (gray, OUT)—assessed separately for quiescent (squares) and energetic regions (diamonds), and for the ALL case also for the entire SO (dots).

estimated recently at $\approx$ 15 W m^{-2} K^{-1} for the SO by *Hausmann et al.* [2016]. It would be interesting to further examine the effects of this small eddy rectification of the surface mixed layer on biogeochemical processes, e.g., via its modification of light availability.

4.2. Eddy Contribution to SO Mixed-Layer Depth Variability

The seasonal cycle of variance of the SO mixed-layer depth field, as measured by the standard deviation of the departures of h from its seasonal climatology $\bar{h}$, $\sigma(h')$, taken across all available Argo profiles collected in a given month of the year (Figure 7b, black dots), is characterized by departures of small magnitude in the summer time, at $\sigma(h') \approx 20$ m. Magnitudes of variability slowly increase during fall and winter to peak at $\sigma(h') \approx 70$ m in September, followed by a quick drop in variance during November and December. Overall, the level of variance in the SO mixed-layer depth field thereby follows the seasonal cycle of its climatological mean, i.e., there is less variance around shallow climatological summer mixed-layer depths, and more variance around the deep winter depths. During most of the year the level of variability thus lies at typically a quarter to a half of the climatological depth. Interestingly, this ratio $\sigma(h')/\bar{h}$ rises to larger values ($\approx$ 0.6–0.8) during the quick shallowing of climatological mixed layers in spring (October–December), possibly reflecting interannual variability in the timing of the onset of this abrupt shallowing.

To assess how the presence of mesoscale eddies contributes to this cycle of SO mixed-layer depth variance, the ensemble of Argo profiles is divided into groups depending on distance to the closest surrounding eddy center. Here each Argo profile is associated with only one single eddy snapshot whose center lies closest to the profile's location. The resulting distribution of the distance to the center of the respectively closest eddy snapshot, $r_{sp-\min}$, identified during the same week ($|\delta t_{sp}| \leq 4$ days), normalized by that eddy snapshot's radius r_e, is displayed in Figure 7a. It reveals that, most frequently, profiles are collected at a distance of 1–1.5 eddy radii from the closest eddy center. 15% of all profiles are collected at a distance to the closest eddy center of less than $\frac{r_{sp-\min}}{r_e}=0.75$, and are thus located within eddy cores. About 10% of profiles are located outside the zone of direct influence of a surrounding eddy, defined here as $\frac{r_{sp-\min}}{r_e} > 2.5$. The remainder of profiles is collected within the periphery of the eddy closest to them in the same week ($0.75 < \frac{r_{sp-\min}}{r_e} \leq 2.5$).

The seasonal cycle of mixed-layer depth variance, assessed separately for these three groups of Argo profiles, collected within eddy cores, eddy peripheries, and outside the zone of eddy influence, is displayed in Figure 7b (by red, green, and grey symbols, respectively), separately for profiles collected only in the South

Pacific quiescent regions (squares) and the ACC energetic regions (diamonds). In quiescent regions, mixed-layer depth variance is reduced compared to its all SO level all year round, with $\sigma(h')$ varying from 10 m in the summer time to a peak at 40 m during September. Here no noticeable difference in h' variance between profiles located within and outside of eddy cores is observed. This suggests that quiescent region eddies do not contribute significantly to setting the level of mixed-layer depth variance there.

In energetic regions (black diamonds), mixed-layer depth variability is larger than in the all SO ensemble (black dots), by up to $\approx$ 20 m during late winter. Here throughout the year, h' variance is significantly larger in the ensemble of profiles collected within eddy cores (red diamonds) compared to those in eddy peripheries (green diamonds), with those outside the zone of direct eddy influence (gray diamonds) featuring even smaller h' variance. This observed enhancement of mixed-layer depth variance amongst profiles within eddy cores compared to those taken outside of direct eddy influence amounts to $\approx$ 20 m during the transition seasons, and is particularly striking from mid-winter through mid-spring (August–November), when the difference in $\sigma(h')$ between the two ensembles reaches $\approx$ 30–45 m. In energetic regions, mixed-layer depth variability, evaluated using all profiles, peaks in October, as it does amongst profiles within energetic eddy cores (at $\sigma(h') \approx$ 110 m). In contrast, the peak of h' variability occurs earlier, in September, amongst profiles outside eddies in energetic regions (at $\approx$ 65 m) and also in quiescent regions (at $\approx$ 40 m).

Together these findings suggest that the presence of mesoscale eddying features and their signatures in mixed-layer depth may, (1) augment the variance of the SO mixed-layer depth field, (2) strengthen the spatial gradient of the SO mixed-layer depth variance, by contributing to its observed increase from quiescent gyres toward the regions of intense eddy variability along the ACC and western boundary current systems, (3) intensify the seasonal cycle of the SO mixed-layer depth variance, by contributing to its observed peak in the winter time, and (4) possibly delay the timing of peak mixed-layer depth variance along the ACC from the end of winter (September) to the beginning of spring (October).

4.3. Eddy Modulation of the Occurrence Frequency of Deep SO Winter Mixed Layers

Here we take a closer look at the distribution of mixed-layer depths in late winter (ASO) along the eddy-intense energetic regions of the SO and assess a possible contribution by the presence of eddies to the deep tail of this distribution.

Amongst all profiles taken in this region and season, with an average depth $h \approx$ 150 m, the distribution of mixed-layer depth is strongly skewed, characterized by frequent shallower than average events and less frequent deeper-than-average events with mixed layers deeper than 200, 300, 400, 500 m, and even occasionally in excess of 600 m (see Figure 8, numbers at the panel top). To evaluate the role eddies play in setting the shape of this distribution and the occurrence of deeper than average events, this ensemble of energetic-region late-winter profiles is divided into groups depending on the profiles' distance to the closest neighboring eddy center, as in Figure 7 above. Of the total number of profiles (slightly more than 10,000), $\approx$ 5% (500 profiles) are collected outside the zone of influence of the nearest eddy, 75% (7500 profiles) within the periphery of the nearest eddy, and 20% (2000 profiles) within eddy cores, with roughly 10% (1000 profiles) in each cyclones and anticyclones (see Figure 8, horizontal lines). For mixed layers shallower than 300 m, eddy peripheries and regions outside of direct eddy influence (Figure 8, green and gray curves) account for a fraction of observations that is roughly equal to the total fraction of profiles in those categories irrespective of the measured h (green and gray lines). However, in the deep tail of the distribution, that is for mixed layers deeper than 300 m, eddy peripheries and regions outside eddy influence account for a systematically smaller fraction of observations than their share of the total number of profiles, and this fraction decreases further on moving toward bins of deeper mixed-layer depth.

As expected from the eddy-induced perturbations in mixed-layer depth, the fraction of observations in bins of h accounted for by profiles located within cyclonic and anticyclonic eddy cores (blue and red curves in Figure 8) reverses between the average mixed-layer depth for cyclones and anticyclones (blue and red vertical bars in Figure 8). For shallower h, cyclonic eddy cores account for a slightly larger fraction of observations than their share of the total number of profiles (blue line), anticyclonic eddy cores for a smaller one. In contrast, for deeper h, cyclones account for less than their share and anticyclones for significantly more. Strikingly, anticyclonic eddy cores, although representing only 10% of the total number of profiles, account for between 20% and 45% of profiles with mixed layers deeper than 300 m. Anticyclonic eddy cores thus clearly contain a disproportionate fraction of late-winter mixed layers deeper than $\approx$ 250 m measured by

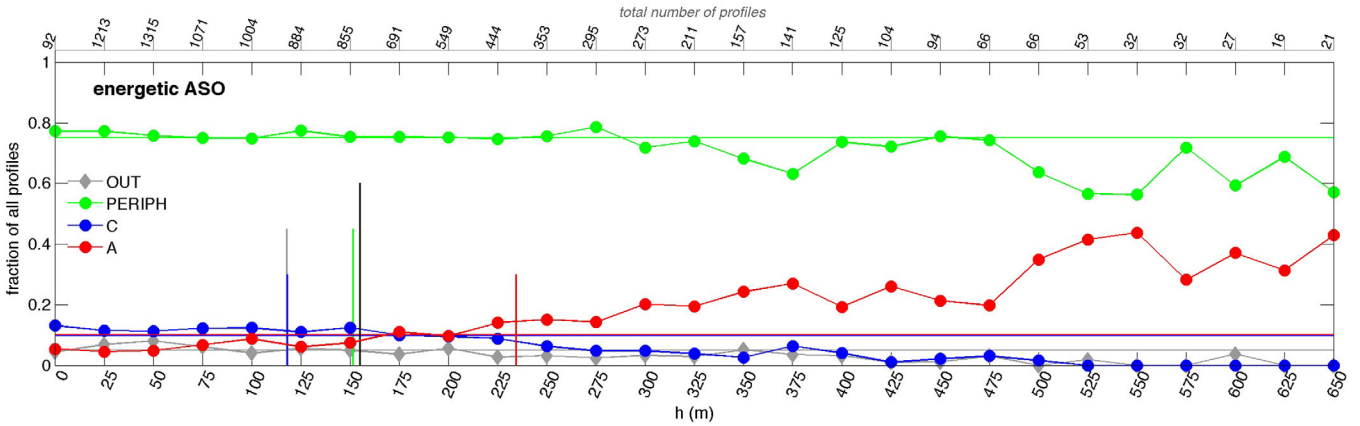

Figure 8. Eddy contribution to the late-winter mixed-layer depth distribution in the SO energetic regions. Fraction of the total number of profiles within cyclonic eddy cores (blue, C), anticyclonic eddy cores (red, C), eddy peripheries (green, PERIPH), and outside the zone of direct eddy influence (gray, OUT) by bins of late-winter (ASO) mixed-layer depth h (horizontal axis). Horizontal lines indicate the fraction of profiles in these different groups irrespective of the value of h measured. Profile groups are defined as in Figure 7, and vertical lines indicate their mean h. The black vertical line indicates the mean h across all profiles, and the total number of profiles for each bin of h is indicated in the top of the panel.

Argo profiles in the energetic ACC region. Cyclones account for a negligible fraction of the deepest mixed layers observed, especially at depth in excess of 400 m.

Together eddy cores of both polarities thus represent more than their share of profile numbers in the deep tail of the h distribution. Eddy cores account for about 20% of total profiles in this region and season, but for $\approx$ 30% of profiles measuring mixed layers deeper than 300 m, and $\approx$ 35% of profiles with mixed layers deeper than 500 m. These observations thus suggest that mesoscale eddies, via the anticyclonic part of their population, enhance the occurrence frequency of late-winter and early-spring SO mixed-layer depth events deeper than the regional and seasonal climatology.

Note that the deep events considered here are rare. Thus, even if eddies play a significant role in modulating the occurrence frequency of such deep events (as suggested here), their role in shaping the average depth of the climatological winter mixed layer is likely small (as discussed in section 4.1).

Finally, we note that the difference between the average mixed-layer depth in anticyclones and cyclones, $h_A - h_C$ in Figure 8, is somewhat larger than the difference in the eddy anomaly signals, $h'_A - h'_C$ in Figure 4b. As further discussed in supporting information Note S3, this reflects residuals of the eddy signal partitioned into the profiles' mixed-layer depth climatologies rather than anomalies (see Figure S5).

5. Conclusions

This study combines a decade of joint Argo profile surface mixed-layer depths with multi-mission satellite altimetry-derived mesoscale eddy data (locations, amplitude, and radii), to identify and document systematic eddy signals in the SO surface mixed-layer depth field. The eddy mixed-layer depth anomalies h', departing from the seasonal climatology $\bar{h}$, are on average shallow in cyclones, deep in anticyclones, and systematically increase in magnitude with eddy amplitude. They are small in the quiescent gyre interiors of the southern hemisphere ocean basins, and reach large amplitudes over the energetic SO western boundary current systems and the ACC path. Eddy mixed-layer depth signatures are characterized by a large seasonal modulation in amplitude, roughly following the seasonal cycle of climatological SO mixed-layer depth: eddy h' are weak in the summer time, increase during the fall, and peak in late winter/early spring, which is during and somewhat after the time the deepest climatological mixed layers are attained in the SO. Composite eddy h' are largest at the eddy centers and on average decay with increasing radial distance. In the average across eddy cores, and at their late winter peak in August-September-October (ASO), they amount to typically -8 m versus $+12$ m over cyclones versus anticyclones in the South Pacific quiescent region, and to -30 m versus $+60$ m along the SO energetic regions. These correspond to late-winter peak composite differences in the eddy signal between anticyclones and cyclones of 20 and 90 m, respectively.

The differences in mixed-layer depths between cyclones and anticyclones found here in the South Pacific (winter peak difference of $\approx$ 20 m) are comparable in their magnitude and seasonal modulation to those documented for the South Indian subtropical gyre by *Gaube et al*. [2013] and *Dufois et al*. [2014]. Moreover, recently *Dufois et al*. [2016] computed eddy-driven perturbations to mixed-layer depth for the subtropical gyres of the world ocean (within the latitude range of $\approx$ 10°–35° N,S) finding comparable winter peak differences of $\approx$ 30 m or less. Compared to the h' signal of these subtropical gyre eddies, the present study documents about four times larger eddy mixed-layer depth perturbations in the energetic ACC and SO western boundary current regions (late-winter peak difference of $\approx$ 90 m), where eddying circulations themselves are roughly four times more intense.

The eddy mixed-layer depth signatures presented here can provide observational benchmarks for eddy-resolving modeling process studies. These in turn will be helpful to provide quantitative insight into the mechanisms via which eddies perturb mixed-layer depths. These include eddy modulation of stratification and shear (geostrophic, and due to internal waves, e.g., *Klein and Hua* [1988] and *Kunze* [1985]), as well as coupling of eddy perturbations in surface flow and temperatures to air-sea fluxes of momentum and heat [*Dewar and Flierl*, 1987; *Williams*, 1988; *Chelton et al*., 2004; *O'Neill et al*., 2012]. Further observational analysis, combining mixed-layer depth with eddy signatures in other fields at the ocean surface and also through the atmospheric boundary layer [*Hausmann and Czaja*, 2012; *Frenger et al*., 2013; *Villas Bôas et al*., 2015], as well as making use of the full information contained in the Argo archive to establish the SO eddy signatures deeper in the water column, will contribute to assessing the mechanisms at play. The latter endeavor will also help to further differentiate meander-type eddying flow fields from highly nonlinear vortices, both of which are considered amongst the mesoscale eddy features investigated in the current study. The latter can advect and trap the surface and mixed-layer water mass properties of their location of origin across the large (mixed-layer depth) gradient across the ACC and SO current fronts [e.g., *Ring Group*, 1981; *Dewar*, 1986], thereby possibly contributing to the large eddy mixed-layer depth perturbations observed in these regions. It will be interesting to assess the mixed-layer depth signatures and the respective contributions to SO mixed-layer depth variability separately for these two types of eddying features, as well as study their evolution throughout their lifetimes.

This study documents a systematic asymmetry across SO eddies, characterized by larger amplitude deep mixed-layer depth anomalies in anticyclones versus less intense shallow anomalies in cyclones. This asymmetry in the amplitude of mixed-layer depth anomalies between cyclones and anticyclones is itself largest during fall and winter and along the energetic regions of the SO. It is not accounted for by asymmetries in the amplitude of the underlying eddying circulations. Interestingly, such an asymmetry is also absent in the eddy signatures in sea surface temperature and air-sea heat fluxes [*Hausmann and Czaja*, 2012; *Villas Bôas et al*., 2015]. The mechanism at the origin of this asymmetric eddy perturbation to mixed-layer depth remains to be further examined. A likely candidate seems to be the combination of opposing impacts of anticyclones and cyclones on stratification in the presence of the sea surface, with the enhancement of geostrophic shear in eddies of both polarities. For a given amplitude of turbulent kinetic energy input by, e.g., atmospheric forcing and given amplitude of eddy perturbations in stratification, this combination leads to a larger surface-layer mixing efficiency, as measured, e.g., by the Richardson number, in anticyclones compared to cyclones. Possible enhancement of shear due to asymmetric internal wave presence in anticyclones [*Kunze*, 1985] may further bias the surface mixing efficiency toward larger values in anticyclones. Idealized eddy-resolving ocean modeling studies could be used to investigate this mechanism, which does not involve eddy-atmosphere coupling.

The net signal that results from the asymmetric perturbations to mixed-layer depth in eddy cores along the ACC region in late winter detected here amounts to typically $+15$ m. With a fraction of time and space of the SO covered by eddy cores of approximately 20%, this study suggests a small impact of eddies on deepening the climatological mean SO winter mixed layer. As discussed, extracting any such rectified eddy signal from observations is not straightforward, as available observed long-term means already contain any such signal if it exists. To address the question of a rectified eddy contribution quantitatively, dedicated high-resolution model experiments are necessary. These will also be instrumental to further clarify the link between the mesoscale mixed-layer depth signals documented here and smaller scale/sub-mesoscale mixed-layer instabilities and their contribution to mixed-layer re-stratification, as documented in various recent modelling studies and also from observations [e.g., *Thompson et al*., 2016; *Johnson et al*., 2016]. Here

it is worthwhile to recall that Argo profile coverage, although representing a step-change in our observing capacity and knowledge of the SO through all seasons, remains comparatively scarce and samples only ≈ 5% of the cores of all eddying features identified in satellite altimetry. Moreover, satellite altimetry itself is limited in spatial resolution, capturing only well-formed mesoscale eddies, with the smaller scales of the mesoscale spectrum remaining at present inaccessible to systematic basin-wide observational studies [e.g., *Chelton et al*., 2011].

This study shows that the variability of mixed-layer depths is enhanced within eddy cores compared to their surroundings in the eddy-rich SO western boundary current systems and along the ACC, and in particular during late winter. Eddies, via the anticyclonic component of their population, are found to enhance the occurrence of deeper than climatological late-winter mixed-layer events. The presence of the eddy perturbations to the SO mixed-layer depth field and its level of variability, documented here, allows the surface mixed layer to intermittently access depths deeper than its climatology and may thereby impact the large-scale seasonal-average temperature, carbon and nutrient concentrations of the SO mixed layer, with possible effects on air-sea fluxes of heat and carbon. Eddies may in this way modulate the average nutrient availability in late winter and early spring in the eddy-rich regions of the SO, with possible impacts on phytoplankton biomass and its blooms, which are observed to onset and peak across the circumpolar SO during late winter, spring, and early summer [*Thomalla et al*., 2011]. Moreover, eddy h', via their anticipated correlation to eddying surface flow anomalies and spatial gradients in both, are directly linked to eddy-driven subduction/obduction, and thus the ventilation and formation of water masses in the SO. In this regard, it would be fascinating to build upon the eddy mixed-layer depth signals characterized here to provide a direct observational estimate of the eddy-driven fluid exchange between the surface layer in regular contact with the atmosphere and the permanent thermocline below, whose assessment so far relies on simple parameterizations relating to estimated eddy diffusivities and large-scale observations of stratification [*Sallée et al*., 2010a; *Sallée and Rintoul*, 2011].

Acknowledgments

We are grateful to Dudley Chelton and colleagues for providing the eddy data set, available at http://cioss.coas.oregonstate.edu/eddies, as well as to James Holte and colleagues for providing Argo mixed-layer depths, available at http://mixedlayer.ucsd.edu, and discussion with H. Song. The Ssalto/Duacs altimeter products were distributed by Aviso (www.aviso.altimetry.fr). U.H. would like to thank Amala Mahadevan and Mick Follows for helpful discussions and J.B. Sallée for an earlier investigation into this topic. The authors furthermore acknowledge support from NSF via the MOBY project investigating the impacts of ocean eddies on biogeochemical cycles. In addition, DJM also acknowledges support from NASA.

References

Chelton, D. B., M. G. Schlax, M. H. Freilich, and R. F. Milliff (2004), Satellite measurements reveal persistent small-scale features in ocean winds, *Science*, *303*(5660), 978–983.

Chelton, D. B., M. G. Schlax, and R. M. Samelson (2011), Global observations of nonlinear mesoscale eddies, *Prog. Oceanogr.*, *91*(2), 167–216.

de Boyer Montégut, C., G. Madec, A. S. Fischer, A. Lazar, and D. Iudicone (2004), Mixed layer depth over the global ocean: An examination of profile data and a profile-based climatology, *J. Geophys. Res.*, *109*, C12003, doi:10.1029/2004JC002378.

Dewar, W. K. (1986), Mixed layers in Gulf Stream rings, *Dyn. Atmos. Oceans*, *10*(1), 1–29.

Dewar, W. K., and G. R. Flierl (1987), Some effects of the wind on rings, *J. Phys. Oceanogr.*, *17*(10), 1653–1667.

Dong, S., J. Sprintall, S. T. Gille, and L. Talley (2008), Southern Ocean mixed-layer depth from Argo float profiles, *J. Geophys. Res.*, *113*, C06013, doi:10.1029/2006JC004051.

Dufois, F., N. J. Hardman-Mountford, J. Greenwood, A. J. Richardson, M. Feng, S. Herbette, and R. Matear (2014), Impact of eddies on surface chlorophyll in the South Indian Ocean, *J. Geophys. Res. Oceans*, *119*, 8061–8077, doi:10.1002/2014JC010164.

Dufois, F., N. J. Hardman-Mountford, J. Greenwood, A. J. Richardson, M. Feng, and R. Matear (2016), Anticyclonic eddies are more productive than cyclonic eddies in subtropical gyres because of winter mixing, *Sci. Adv.*, *2*, e1600282, doi:10.1126/sciadv.1600282.

Ferrari, R., and C. Wunsch (2009), Ocean circulation kinetic energy: Reservoirs, sources, and sinks, *Annu. Rev. Fluid Mech.*, *41*(1), 253–282.

Frenger, I., N. Gruber, R. Knutti, and M. Muennich (2013), Imprint of Southern Ocean eddies on winds, clouds and rainfall, *J. Geophys. Res. Oceans*, *6*, 608–612, doi:10.1038/NGEO1863.

Frenger, I., M. Muennich, N. Gruber, and R. Knutti (2015), Southern Ocean eddy phenomenology, *J. Geophys. Res. Oceans*, *120*, 7413–7449, doi:10.1002/2015JC011047.

Gaube, P., D. B. Chelton, P. G. Strutton, and M. J. Behrenfeld (2013), Satellite observations of chlorophyll, phytoplankton biomass, and Ekman pumping in nonlinear mesoscale eddies, *J. Geophys. Res. Oceans*, *118*, 6349–6370, doi:10.1002/2013JC009027.

Gaube, P., D. J. McGillicuddy, D. B. Chelton, M. J. Behrenfeld, and P. G. Strutton (2014), Regional variations in the influence of mesoscale eddies on near-surface chlorophyll, *J. Geophys. Res. Oceans*, *119*, 8194–8220, doi:10.1002/2014JC010111.

Gill, A. E., J. S. A. Green, and A. J. Simmons (1974), Energy partition in large-scale ocean circulation and production of mid-ocean eddies, *Deep Sea Res. Oceanogr. Abstr.*, *21*(7), 499–528.

Hausmann, U., and A. Czaja (2012), The observed signature of mesoscale eddies in sea surface temperature and the associated heat transport, *Deep Sea Res. Part I*, *70*, 60–72, doi:10.1016/j.dsr.2012.08.005.

Hausmann, U., A. Czaja, and J. Marshall (2016), Estimates of air-sea feedbacks on sea surface temperature anomalies in the Southern Ocean, *J. Clim.*, *29*, 439–454, doi:10.1175/JCLI-D-15-0015.1.

Holte, J., and L. Talley (2009), A new algorithm for finding mixed layer depths with applications to Argo data and Subantarctic Mode Water formation, *J. Atmos. Oceanic Technol.*, *26*, 1920–1939, doi:10.1175/2009JTECHO543.1.

Holte, J., J. Gilson, L. Talley, and D. Roemmich (2010), Argo mixed layers. [Available at http://mixedlayer.ucsd.edu.]

Johnson, L., C. M. Lee, and E. A. d'Asaro (2016), Global estimates of lateral springtime restratification, *J. Phys. Oceanogr.*, *46*, 1555–1573, doi:10.1175/JPO-D-15-0163.1.

Joyce, T. M., and M. C. Stalcup (1985), Wintertime convection in a Gulf Stream warm core ring, *J. Phys. Oceanogr.*, *15*(8), 1032–1042.

Joyce, T. M., S. L. Patterson, and R. C. Millard Jr. (1981), Anatomy of a cyclonic ring in the Drake Passage, *Deep Sea Res. Part A*, *28*(11), 1265–1287.

Klein, P., and B. L. Hua (1988), Mesoscale heterogeneity of the wind-driven mixed layer: Influence of a quasigeostrophic flow, *J. Mar. Res.*, *46*(3), 495–525.
Kunze, E. (1985), Near-inertial wave propagation in geostrophic shear, *J. Phys. Oceanogr.*, *15*, 544–656.
Mahadevan, A. (2016), The impact of submesoscale physics on primary productivity of plankton, *Annu. Rev. Mar. Sci.*, *8*, 161–184.
McGillicuddy, D. J. (2016), Mechanisms of physical-biological-biogeochemical interaction at the oceanic mesoscale, *Annu. Rev. Mar. Sci.*, *8*, 125–159.
O'Neill, L. W., D. B. Chelton, and S. K. Esbensen (2012), Covariability of surface wind and stress responses to sea–surface temperature fronts, *J. Clim.*, *25*, 5916–5942, doi:10.1175/JCLI-D-11-00230.1.
Ring Group (1981), Gulf Stream cold-core rings: Their physics, chemistry, and biology, *Science*, *212*(4499), 1091–1100.
Sallée, J. B., and S. R. Rintoul (2011), Parameterization of eddy-induced subduction in the Southern Ocean surface-layer, *Ocean Modell.*, *39*(1–2), 146–153.
Sallée, J. B., K. Speer, S. R. Rintoul, and S. Wijffels (2010a), Southern Ocean thermocline ventilation, *J. Phys. Oceanogr.*, *40*, 509–529, doi:10.1175/2009JPO4291.1.
Sallée, J. B., K. Speer, S. R. Rintoul, and S. Wijffels (2010b), Zonally asymmetric response of the Southern Ocean mixed-layer depth to the Southern Annular Mode, *Nat. Geosci.*, *3*, 273–279, doi:10.1038/NGEO812.
Schmidtko, S., G. C. Johnson, and J. M. Lyman (2013), MIMOC: A global monthly isopycnal upper-ocean climatology with mixed layers, *J. Geophys. Res. Oceans*, *118*, 1658–1672, doi:10.1002/jgrc.20122.
Schmitt, R. W., and D. B. Olson (1985), Wintertime convection in warm-core rings: Thermocline ventilation and the formation of mesoscale lenses, *J. Geophys. Res.*, *90*, 8823–8837.
Scott, R. B., and F. Wang (2005), Direct evidence of an oceanic inverse kinetic energy cascade from satellite altimetry, *J. Phys. Oceanogr.*, *35*(9), 1650–1666.
Thomalla, S. J., N. Fauchereau, S. Swart, and P. M. S. Monteiro (2011), Regional scale characteristics of the seasonal cycle of chlorophyll in the Southern Ocean, *Biogeosciences*, *8*, 2849–2866.
Thompson, A. F., A. Lazar, C. Buckingham, A. C. N. Garabato, G. M. Damerell, and K. J. Heywood (2016), Open-ocean submesoscale motions: A full seasonal cycle of mixed layer instabilities from gliders, *J. Phys. Oceanogr.*, *46*, 1285–1307, doi:10.1175/JPO-D-15-0170.1.
Vastano, A. C., J. E. Schmitz, and D. E. Hagan (1980), The physical oceanography of two rings observed by the Cyclonic Ring Experiment. Part I: Physical structures, *J. Phys. Oceanogr.*, *10*(4), 493–513.
Villas Bôas, A. B., O. T. Sato, A. Chaigneau, and G. P. Castelão (2015), The signature of mesoscale eddies on the air-sea turbulent heat fluxes in the South Atlantic Ocean, *Geophys. Res. Lett.*, *42*, 1856–1862, doi:10.1002/2015GL063105.
Williams, R. G. (1988), Modification of ocean eddies by air-sea interaction, *J. Geophys. Res. Oceans*, *93*(C12), 15,523–15,533.